LA-13566-MS

Issued: May 1999

Calculation of Moments from Measurements by the Los Alamos Magnetospheric Plasma Analyzer

M. F. Thomsen
E. Noveroske
J. E. Borovsky
D. J. McComas

Los Alamos
NATIONAL LABORATORY
Los Alamos, New Mexico 87545

This work was supported by the US Department of Energy, Office of Nonproliferation and National Security.

An Affirmative Action/Equal Opportunity Employer

Calculation of Moments from Measurements
by the Los Alamos Magnetospheric Plasma Analyzer
by

M. F. Thomsen, E. Noveroske, J. E. Borovsky, and D. J. McComas

Abstract

The various steps involved in computing the moments (density, velocity, and temperature) of the ion and electron distributions measured with the Los Alamos Magnetospheric Plasma Analyzer (MPA) are described. The assumptions, constants, and algorithms contained in the FORTRAN code are presented, as well as the output parameters produced by the code.

1. Introduction

Since 1989, Los Alamos National Laboratory has been fielding a set of plasma and energetic particle instruments on a number of geosynchronous satellites. The purpose of these instruments is to monitor the spacecraft environment in support of the spacecraft mission. In addition, the measurements from these environmental monitors provide a near-real-time monitoring capability for space weather observations. Moreover, with simultaneous multipoint measurements and an extensive database, Los Alamos geosynchronous measurements are a rich resource for scientific study of magnetospheric structure and dynamics. The purpose of this report is to document the steps involved in one of the primary analysis tools routinely applied to the geosynchronous plasma data, namely the computation of the plasma moments.

The Magnetospheric Plasma Analyzer (MPA) [Bame et al., 1993; McComas et al., 1993] is a spherical-sector electrostatic analyzer with a bending angle of 60°. The field of view is divided up into six separate but contiguous detectors covering the range of polar angle from ~25° to ~155° with respect to the Earth-pointing spin axis, and the satellite spin allows the instrument to view 360° in azimuth, which is divided into 24 sectors of 15°. Thus in one spin the MPA views ~92% of the unit sphere, divided into six polar by 24 azimuthal view directions. As the spacecraft spins through each 15° azimuthal sector, the MPA plate voltage is swept through 40 logarithmically spaced energy channels ranging from ~40 keV/*e* down to ~1 eV/*e*. A complete three-dimensional (40 energies × 24 azimuths × 6 polar angles) distribution is obtained in one ~10-s spin. As described more fully in Bame et al. [1993], a full MPA data cycle contains several different data types, with the sequence repeated at 86-s intervals. The data types and the order in which they are accumulated are P3,Pθ,E3,E2,Eθ,P3,E2,E2. The moments described here are computed from the three-dimensional distributions P3 (ions) and E3 (electrons); only the first P3 spectrum in an 86-s sequence is used.

From the measurements of each full three-dimensional distribution, various velocity moments are computed, specifically the density, the vector velocity, and the 3-dimensional temperature matrix:

$$n = \int f(\mathbf{v})\, d^3\mathbf{v} \quad , \tag{1a}$$

$$\mathbf{V} = (1 / n) \int \mathbf{v}\, f(\mathbf{v})\, d^3\mathbf{v} \quad , \tag{1b}$$

$$\mathbf{T} = (1 / n) \int m\, (\mathbf{v}-\mathbf{V})\, (\mathbf{v}-\mathbf{V})\, f(\mathbf{v})\, d^3\mathbf{v} \quad , \tag{1c}$$

where $f(\mathbf{v})$ is the measured phase space density at a particle velocity $\mathbf{v}$ and m is the particle mass (the analyzer measures only energy per charge, so our routine analysis of ion measurements assumes that all the positively charged particles are protons). The purpose of this report is to document the algorithms for computing these moments from the measured count rates. The algorithms have been implemented in a FORTRAN code that is routinely applied to all MPA data.

The steps involved in the computation of MPA moments and the sections in which they are discussed are the following:

- 2a. Initialization
- 2b. Filter for incomplete and bad data
- 2c. Decompression
- 2d. Dead-time correction
- 2e. Replacement of counts from bad detectors
- 2f. Determination of ephemeris and spin period
- 2g. Determination of look angles associated with each sample
- 2h. Background subtraction
- 2i. Determination of spacecraft potential
- 2j. Exclusion of trapped photoelectron contamination
- 2k. Computation of flux and phase space density matrices
- 2l. Correction of energies for the spacecraft potential
- 2m. Computation of sums
- 2n. Interpolation across polar gaps
- 2o. Combination of sums to yield moments

The contents of the various output data files are described in Section 3.

2. Computational Steps

2a. Initialization

To facilitate change control, the detector characteristics and constants used in the moments calculation are collected in a single subroutine ("AMPA_STATUS") that is accessed by the main moments code. This subroutine contains information from laboratory

calibrations, on-orbit calibrations, and ongoing monitoring of instrument state-of-health. Because some of the parameters vary with time over the course of the various satellite histories, the call to the subroutine specifies the satellite and the date. The parameters specified in the subroutine are the following:

Channel edge energies. These energies are based on laboratory calibrations, with interpolation or extrapolation of measured values to fill in for channels not directly measured. They are listed here in Table 1. As indicated by the shading in the table, the energy values of the lowest five ion channels on 1991-080 are not deemed to be reliable, and those channels are not included in the moments calculations described here.

Geometric factors. The geometric factors are calculated with a code that numerically integrates the transmission characteristics of a spherical section electrostatic analyzer, as detailed by Gosling et al. [1984]. The computed values are very close to those derived using the approximate formula for G given as Equation P-3 in Gosling et al. The values for the six detectors are (3.26×10^{-4}, 4.90×10^{-4}, 5.74×10^{-4}, 5.74×10^{-4}, 4.90×10^{-4}, 3.26×10^{-4}) cm^2 sr.

Detector angular ranges. The ranges of polar angle response of MPA have been determined by laboratory tests and closely confirmed by the same numerical calculation that produced the geometric factors. The response is shown by Bame et al. [1993]. While the true angular response has been incorporated into the geometric factors, for the purposes of the moments computation the measured distribution function is assumed to fill contiguous polar angle channels centered on the measured ones. The ranges of polar look angles (θ_{1j}-θ_{2j}) are thus (21°-44°, 44°-67°, 67°-90°, 90°-113°, 113°-136°, 136°-159°). As described more fully below, the unmeasured "polar gaps" of the distribution (within 21° of the spin axis) are filled by interpolation from the measured portions of the distribution.

Valid detectors. For four of the first five MPA instruments that have been launched, one of the six channel-electron-multipliers exhibited a high noise level in early on-orbit operations. In some cases this noisy channel has recovered full functionality over the course of time. The instrument-constants subroutine maintains a time-history of the status of the six detectors on each satellite. As discussed below, the data from malfunctioning detectors can be replaced with valid data interpolated from measurements by the other detectors.

Detector efficiencies. The relative efficiencies of the six channel-electron-multipliers (CEMs) on each MPA instrument are determined from on-orbit measurements

Table 1. Channel Edge Energies

Edge	046 ion	046 elec	095 ion	095 elec	080 ion	080 elec	084 ion	084 elec	97A ion	97A elec
0	43370	44261	43641	47762	49139	46375	48744	47135	46475	47539
1	33353	33865	33508	36316	37638	35412	37137	35849	35488	36214
2	25649	25911	25728	27613	28828	27041	28293	27266	27099	27586
3	19725	19825	19755	20996	22080	20648	21556	20737	20693	21014
4	15169	15169	15168	15964	16912	15767	16423	15772	15802	16008
5	11665	11606	11646	12138	12953	12040	12512	11995	12066	12194
6	8970.9	8880.3	8942.3	9229.6	9921.5	9193.5	9532.5	9123.2	9213.8	9289.0
7	6898.9	6730.0	6866.1	7017.7	7599.2	7020.2	7262.5	6938.8	7035.8	7076.0
8	5350.0	5170.0	5271.9	5336.0	5820.5	5360.6	5533.1	5277.3	5372.6	5390.3
9	4090.0	3970.0	4047.9	4025.0	4365.0	4093.4	4200.0	4000.0	4090.0	4106.1
10	3150.0	3030.0	3108.0	3050.0	3360.0	3120.0	3200.0	3050.0	3130.0	3100.0
11	2410.0	2350.0	2386.4	2325.0	2580.0	2390.0	2450.0	2310.0	2380.0	2400.0
12	1860.0	1790.0	1832.3	1770.0	1980.0	1825.0	1870.0	1770.0	1840.0	1830.0
13	1420.0	1380.0	1406.9	1360.0	1510.0	1396.0	1420.0	1350.0	1400.0	1390.0
14	1090.0	1050.0	1090.0	1040.0	1220.0	1069.0	1090.0	1030.0	1070.0	1050.0
15	832.00	801.00	834.00	793.00	925.00	815.00	825.00	776.00	811.00	796.00
16	649.01	614.00	641.00	602.00	703.00	617.00	626.00	593.00	619.00	607.00
17	505.00	468.00	488.00	460.00	538.00	471.00	480.00	447.00	475.00	468.00
18	385.00	358.00	373.00	347.00	408.00	360.00	365.00	342.00	362.00	353.00
19	295.00	274.00	287.00	264.00	314.00	275.00	276.00	259.00	276.00	270.00
20	226.00	209.00	220.00	200.00	237.00	210.00	211.00	196.00	212.00	207.00
21	173.00	159.00	168.00	152.00	182.00	161.00	161.00	150.60	163.30	159.00
22	133.00	120.00	129.00	114.00	139.00	122.00	124.00	114.80	125.50	121.40
23	103.00	92.100	99.700	87.000	105.00	93.600	93.600	88.900	97.600	94.800
24	79.900	70.300	77.200	66.300	80.900	71.900	72.200	67.700	75.700	72.900
25	62.000	57.300	60.500	50.100	61.200	55.200	55.600	51.500	59.100	55.000
26	48.200	43.500	47.100	38.100	45.800	42.500	42.700	39.200	45.900	43.800
27	37.500	32.700	36.900	28.900	34.500	30.500	33.100	29.800	35.900	33.800
28	29.500	24.500	29.000	21.600	25.500	23.100	26.200	22.700	29.300	26.700
29	23.200	19.600	22.800	16.300	18.500	17.800	20.400	17.700	22.800	20.000
30	18.400	15.000	18.200	11.700	12.900	15.100	15.780	13.300	18.450	14.730
31	14.600	11.300	14.800	8.6500	9.0000	12.800	12.280	11.200	14.810	12.520
32	11.800	8.3500	12.200	6.6300	6.1000	9.5000	10.490	8.8000	11.800	10.550
33	9.5300	6.0000	10.000	4.9700	4.1000	7.2000	8.1000	6.8000	9.1000	7.6200
34	7.6400	4.2800	8.3700	3.8500	2.3000	5.3500	6.1200	5.3000	6.8000	5.0300
35	6.2000	2.9308	7.0300	3.1500	1.0000	3.8100	4.7700	4.4000	5.0000	3.8800
36	5.1100	2.0538	6.1000	2.5400	0.51535	2.7200	3.9300	3.8000	3.8000	2.7100
37	4.2100	1.4393	5.3000	2.2900	0.25452	1.9000	3.2800	2.7000	2.9000	2.0100
38	3.5700	1.0000	4.3300	1.9000	0.12570	1.0300	2.3000	2.2000	2.2000	1.8000
39	3.0000	0.70678	3.8200	1.6500	0.06207	0.48000	1.2700	1.8000	1.8000	1.0000
40	2.5071	0.49529	3.2466	1.4269	0.03065	0.24743	0.70133	1.4700	1.3503	0.96609

during times of nearly isotropic fluxes, when all the detectors should be exposed to the same incident flux. Only measurements that are well above background, nearly isotropic, and statistically significant are included in the determination. The derivation of the relative efficiencies and their effect on the determination of the symmetry axis of the measured distributions are described in detail by Thomsen et al. [1996]. We assign an absolute efficiency of 0.95 to the most efficient detector in each set of six, and the other values then follow from the measured relative efficiencies. The adopted efficiencies are listed in Table 2.

Table 2. Adopted Efficiencies

Detector	1989-046	1990-095	1991-080	1994-084	LANL-97A
1	0.91	0.95	0.74	0.91	0.92
2	0.82	0.81	0.88	0.95	0.83
3	0.74	0.71	0.82	0.89	0.95
4	0.85	0.91	0.95	----	0.92
5	0.88	0.93	0.86	0.78	0.95
6	0.95	0.95	0.95	0.83	----

Finally, we apply an energy dependence to the CEM efficiencies that, for the electrons, is based on Monte Carlo simulations of secondary electron yield and probability of avalanche formation in the CEMs [H. Funsten, personal communication, 1997] and, for the ions, is based on laboratory measurements [H. Funsten, personal communication, 1996]. The functions adopted for the two species are the following (with energies specified in eV):

$\underline{E_e \leq 800\ eV}$

$$\varepsilon = 0.76017 + 0.0010735\ E_e - 1.8392 \times 10^{-6}\ E_e^2 + 1.091 \times 10^{-9}\ E_e^3$$

$\underline{E_e > 800\ eV}$

$$\varepsilon = 1.834 - 0.2845 \log(E_e)$$

$\underline{\text{All } E_i}$

$$\varepsilon = 0.7205 + 1.180 \times 10^{-3}\ (E_i + 1200)^{0.509}$$

Thus, the best detector is attributed an absolute efficiency of 0.95 at an electron energy of 800 eV and an ion energy of 45 keV.

Highest valid energy level. Over the course of time, the first three MPA instruments showed evidence of degradation of the high-voltage power supply (HVPS). As a consequence of this degradation, the supplies were not able to produce the highest analyzer plate voltages needed to achieve the desired energy coverage, although the lower voltages were nominal. The net effect of the problem is that the top channel(s) on those instruments do not measure fluxes at their nominal energy. The

instrument-constants subroutine maintains a time history of the highest valid energy channel.

2b. Filter for incomplete and bad data

The moments are only computed for records containing both a complete three-dimensional ion spectrum and a complete three-dimensional electron spectrum. Moreover, moments are not computed for records on either side of a data gap, nor for records where more than 10 count-rate words contain fill values. (If 10 or fewer words contain fill values, the fill values are replaced by zeroes in the calculation.) Finally, for records where one or more bad main frames are detected, a cautionary flag is set, but the moments are still computed since the corrupted part of the main frame may or may not be in the MPA 3-D data.

2c. Decompression

The first step in the actual data handling is to reverse the onboard log compression applied to the count rates to reduce the telemetry volume. This reversal is applied in the utility subroutine that retrieves each data record.

2d. Dead-time correction

At high count rates, dead time in the electronics reduces the measured count rate compared to the true rate. This reduction is reversed by applying the expression

$$C = C'/[1 - C' (t_d/\tau)] \quad ,$$

where C' is the number of counts measured in one accumulation interval τ (9 ms), t_d is the relevant dead time (1.2 μs [Bame et al., 1993]), and C is the estimated number of true counts per accumulation interval.

2e. Replacement of counts from bad detectors

As mentioned above, for four of the first five MPA instruments that have been launched to date, one of the six channel-electron-multipliers exhibited a high noise level in early on-orbit operations. In a few cases, this noise gradually disappeared over the course of several months, but in order to take full advantage of the measurements made in the early part of those missions, we replace the contaminated data with values estimated from measurements made by the other detectors.

At energies above ~130 eV for the ions (channels 1-22) and ~40 eV for the electrons (channels 1-26), under the assumption that the distribution is gyrotropic and symmetric in pitch angle, we simply substitute the magnetically conjugate measurements made by the complementary detector (i.e., detectors 1 and 6, 2 and 5, 3 and 4) a half-spin earlier or later:

$$C_{ijk} = C_{i,7-j,k+12} / \varepsilon_{7-j} \quad ,$$

where C_{ijk} is the replacement count rate at the ith energy level and kth azimuth for the (noisy) detector j. The counts at the complementary detector (7-j) are normalized by its relative efficiency, ε_{7-j}.

At lower energies (channels 23-40 for ions and 27-40 for electrons), we use a quadratic interpolation of measurements made by the adjacent detectors. The interpolation scheme depends on which of the detectors is being replaced:

$$C_{ijk} = a\, x_3^2 + b\, x_3 + c \quad ,$$

where

$$a = [(x_2 - x_4) \times y_1 + (x_4 - x_1) \times y_2 + (x_1 - x_2) \times y_4] / D \quad ,$$

$$b = -a\,(x_1 + x_2) + (y_1 - y_2) / (x_1 - x_2) \quad ,$$

$$c = y_1 - a\, x_1^2 - b\, x_1 \quad ,$$

$$D = (x_1 - x_2) \times (x_1 - x_4) \times (x_2 - x_4) \quad .$$

The x_n represent the center polar angles for the various detectors, and the y_n represent the corresponding efficiency-corrected count rates. The x_n and y_n appropriate for the replacement of detectors 2, 3, 4, and 5 are listed in Table 3. For the end detectors (1 and 6), the replacement is simply done using the efficiency-corrected counts of the adjacent detector:

$$C_{i1k} = C_{i2k} / \varepsilon_2$$

$$C_{i6k} = C_{i5k} / \varepsilon_5 \quad .$$

Table 3. Detector Replacement Parameters

Replaced Detector	x_1	y_1	x_2	y_2	x_4	y_4	x_3
2	101.5	C_{i4k} / ε_4	78.5	C_{i3k} / ε_3	32.5	C_{i1k} / ε_1	55.5
3	124.5	C_{i5k} / ε_5	101.5	C_{i4k} / ε_4	55.5	C_{i2k} / ε_2	78.5
4	55.5	C_{i2k} / ε_2	78.5	C_{i3k} / ε_3	124.5	C_{i5k} / ε_5	101.5
5	78.5	C_{i3k} / ε_3	101.5	C_{i4k} / ε_4	147.5	C_{i6k} / ε_6	124.5

We have tested the effect of the replacement schemes on the derived symmetry axis direction by applying the algorithms to data from 1989-046, on which all six CEMs functioned properly, and comparing the resultant tilt angles with the angles derived using the full set of six detectors. The results of these tests are reported in Thomsen et al. [1996].

2f. Determination of ephemeris and spin period

The spin period is determined from succeeding values of the time of zero yaw. Since this difference may represent several spins, the spin period is the zero-yaw difference divided by the integer that yields a value between 9 and 11 seconds. If no zero-yaw information is provided, an algorithm written by S. Maurice is used to derive the time of zero yaw from the sun-sensor pulse and the spacecraft position and measurement epoch.

The satellite ephemeris in geographic coordinates is normally supplied with the data file. However, it is not uncommon for the files to contain no ephemeris information. In this event, the code queries a special database of orbital elements and computes the spacecraft position.

2g. Determination of look angles associated with each sample

The azimuthal look angle of the detectors for each energy level within a sweep is determined from the spin period, the most recent time of zero yaw, and the start time of the main frame containing the top-of-data flag. At the time of zero yaw, the MPA field of view is centered on a roll azimuth of 78.75° relative to the plane containing the spin axis and geographic north. Thus, at any other time t, the MPA roll azimuth relative to north is

$$\phi(t) = 78.75^\circ + 360^\circ\ (t - t_{zero\text{-}yaw})/\ T_{spin} \quad .$$

The look azimuth $\phi_{ik} = \phi(t=t_{ik})$ is assigned to the center of the ith accumulation interval in the kth sweep, with

$$t_{ik}(s) = t_{start} + \Delta t + 0.423\ (k-1) + 0.009\ (i-1) + 0.0045 \quad ,$$

i.e.,

$$\phi_{ik} = 78.75^\circ + 360^\circ\ (t_{ik} - t_{zero\text{-}yaw})/\ T_{spin} \quad . \qquad (2)$$

For data returned since the ground station upgrade in 1995 (archival files ending .bkg_mpa), t_{start} is the start time of data collection of the first scan in an 86-s MPA cycle (ST_GMT_MPA) and $\Delta t = \Delta t_{bkg}$ is the time delay between the start of the current data type and the start of the first P3 accumulation. Table 4 lists the delay time Δt_{bkg} for the eight different data types in an 86-s MPA cycle. Prior to the ground station upgrade in 1995 the

MPA data files had a different format, and the timing was handled slightly differently. In those files, which had names ending in .mpa_e3u, each data type was labeled with its own start time of data reception, which replaced t_{start} in Equation 2, and the delay time $\Delta t=\Delta t_{e3u}$ accounted for the buffering time between the start of the accumulation and the insertion of the data into the telemetry. The delay time Δt_{e3u} for each of the data types is also listed in Table 4.

Table 4. Accumulation Delay Times

Data Type	No. Main Frames	Δt_{bkg} (s)	Δt_{e3u} (s)
P3-1	10	0	-0.002
Pθ	11	10.240	-12.818
E3	10	21.504	-4.162
E2-1	10	31.744	-16.978
Eθ	11	41.984	-10.594
P3-2	10	53.248	-1.938
(wait)	1	-	-
E2-2	10	64.512	-13.730
E2-3	10	74.752	-7.346
(wait)	1	-	-

2h. Background subtraction

Charged particles with sufficiently high energies (typically above ~1 MeV for electrons and 10's of MeV for ions) can penetrate directly through the MPA instrument and be detected by the channel-electron-multipliers. Such energetic populations thus produce a background count rate in the detectors which is independent of the analyzer plate voltage. Since all energy channels have the same accumulation interval, the background counts are independent of energy level to within the statistical variation of finite counts. Empirically, this background is found to vary significantly from detector to detector. To estimate the background for each detector, the spin-averaged count rate is computed for each of the 40 ion energy levels. The lowest of these 40 values is then adopted as the background count rate for that detector:

$$b_j \equiv \min_i \left(\sum_k C_{ijk}\right) / 24 \quad ,$$

and these values are subtracted from each individual sample (C_{ijk}) in the full distribution.

Normally, the fluxes of electrons are high enough that the count rates are dominated by true analyzed electrons, and the background correction described above has very little effect. On rare occasions, however, the electron fluxes become quite low, and the ion-based correction turns out to be an overestimate of the true background in the electron measurements. For such intervals, a separate electron background is computed in complete analogy to the ion background described above, and if that electron background is smaller than twice the corresponding ion-based background, the electron background is used to correct the electron count rates.

To monitor the overall level of the background, we also compute the average background for the 6 detectors:

$$b_{ave} = \sum_j b_j / 6 \quad .$$

Because the background is estimated from the minimum spin-average in the spectrum, it is probably slightly underestimated, and a small background contribution remains in the distributions. The influence of this contribution on the derived low-energy ion density has been examined by Lawrence et al. [1999]. That analysis yielded a threshold expression for the low-energy ion density below which background contamination was likely to be dominating the derived value:

$$n_{lp}(\text{threshold}) = 0.6\, n_{lp0} \sqrt{b_{ave}} \quad ,$$

where n_{lp} is the computed low-energy ion density, n_{lp0} is the density that would result if every bin had exactly one count in it, and b_{ave} is the detector-averaged background discussed above. The values of n_{lp0} for the first 5 MPAs are given in Table 5.

Table 5. Background Densities

Spacecraft	n_{lp0} (cm^{-3})
1989-046	2.85
1990-095	2.36
1991-080	4.97
1994-084	5.74
LANL-97A	4.77

2i. Determination of spacecraft potential

The level of surface charging of a satellite is determined by the balance of several different currents. These currents include the photoelectron current, the current due to ambient electrons, the current due to ambient ions, and the current due to ejected secondary electrons. If these currents are unbalanced, the spacecraft will charge up, enhancing some of the currents and reducing others until they are in balance again. During substorm injections, the flux of hot electrons increases dramatically, causing a satellite to charge to large negative potentials relative to the ambient medium. As a consequence, ambient ions are accelerated toward the satellite, arriving with energies at and above the spacecraft potential. Similarly, ambient electrons are decelerated and arrive at the satellite with energies lower than their original values. To calculate the moments of these populations it is necessary to correct for this acceleration or deceleration; hence, it is necessary to determine the spacecraft potential relative to the ambient plasma.

If there is a sufficient density of low-energy ambient ions, acceleration through the spacecraft sheath produces a detectable narrow peak in the ion energy distribution at the spacecraft potential, with only background counts below that energy. This signature provides a direct measure of the spacecraft potential. The algorithm employed in the moments code for identifying the spacecraft potential therefore begins with a search for such a peak in the ion spectrum. Specifically, the code searches the spin-averaged ion spectrum below 9 keV for the largest logarithmic increase in counts from one energy level to the next. To be a valid determination of the potential, this jump must be at least a factor of 2, and the counts at the top of the jump must be at least 2. If the total counts in the highest 10 electron energy channels do not exceed 500 (i.e., if there are low electron fluxes in the main surface-charging energy range), the search is only conducted below 150 eV. When the satellite is located within an hour of local midnight (and could thus be in eclipse), the search is restricted to the lower energies when the total counts in the highest 10 electron channels are below 300.

If a valid ion peak is found in this manner, the energy corresponding to the channel where the jump occurs is taken to be the spacecraft potential. If no such peak can be found, there are two other possible outcomes: (1) if the counts in the lowest ion energy channel exceed the background by at least 5 standard deviations, the spacecraft potential is taken to be zero or (2) if neither a valid peak nor a "real zero" is found, an iterative approach is used to estimate the spacecraft potential based on the derived moments, specifically the average total electron temperature, which is estimated from the hot electron density and temperature and the low-energy ion density. This iteration is based on the empirical relationship found between the average electron temperature derived from these parameters and the spacecraft potential derived from observed valid ion peaks. This

relationship is illustrated in Figure 1, where the average electron temperature shown there is defined as

$$T_{e,ave} \equiv [(n_{lp} \times 5.0\ eV) + (n_{he} \times T_{he})] / (n_{lp} + n_{he}) \quad .$$

In this expression n_{lp} is the derived low-energy ion density (used as a proxy for the low-energy electron density), the low-energy electron temperature is approximated as 5.0 eV, and n_{he} and T_{he} are the derived hot electron density and temperature, respectively. The functional form adopted to represent the relationship shown in Figure 1 is

$$-\Phi_{sc} = A + B \times (T_{e,ave} / T_o)^D \quad , \tag{3}$$

where the fit parameters A, B, T_o, and D are determined for each satellite and listed in Table 6.

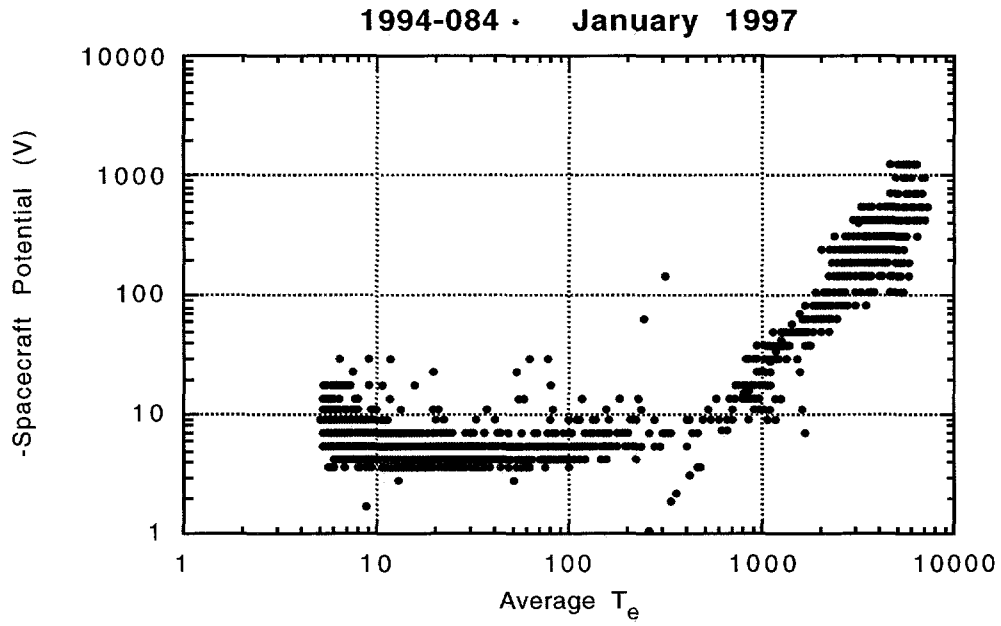

Figure 1. Empirical relationship between the negative of the measured spacecraft potential and the average electron temperature of the ambient plasma.

In the iterative procedure used to determine the spacecraft potential in the absence of a valid ion peak or a real zero, the spacecraft potential is initially assumed to be zero and the moments are calculated accordingly. Then $T_{e,ave}$ is estimated based on the resulting values of n_{lp}, n_{he}, and T_{he}. This $T_{e,ave}$ is then used to make a new estimate of Φ_{sc} through Equation 3. In turn, this new Φ_{sc} is used to recalculate the moments. The procedure

repeats until the estimated Φ_{sc} converges to within 10% of its previous value or for a maximum of 5 iterations.

2j. Exclusion of trapped photoelectron contamination

Under conditions of surface charging in sunlight, the satellites carrying the MPA instruments typically charge differentially, so that some parts are at more negative potentials than other parts. This differential charging creates potential barriers that can trap photoelectrons and locally produced secondary electrons, even though on the whole the satellite is charged to large negative potentials such that low-energy electrons should be

Table 6. Parameters Relating Φ_{sc} and $T_{e,ave}$

Spacecraft	A	B	T_o	D
1989-046	3.9	0.015025	46.074	2.4257
1990-095	4.8	0.015025	46.074	2.4257
1991-080	3.9	0.015025	46.074	2.4257
1994-084	4.3	0.015025	46.074	2.4257
LANL-97A	7.9	0.015025	46.074	2.4257

accelerated away from the spacecraft. This effect can be clearly seen as intense fluxes of lower-energy electrons, typically below about 30 eV but sometimes extending as high as 200 eV or more, during times of strong surface charging. These intense fluxes of electrons can seriously affect the computed moments of the high-energy electron population, which nominally includes all of the channels above about 30 eV, and care must be taken to exclude contaminated channels from the calculation. Our main concern is not so much to know the value of the barrier potential itself but to ensure that no contamination from trapped electrons can affect the higher-energy moments. Therefore, the code employs an algorithm that looks for the telltale rise in electron counts at low energies as the signature of barrier-trapped electrons. Specifically, since we are only worried about contamination above the nominal threshold of 30 eV, the code looks for a minimum in the spin-averaged electron count rate between channel 18 (~400 eV) and channel 28 (~30 eV). If no minimum is found, the computation of the high-energy electron moments extends down to 30 eV. If a minimum is found, and if there are sufficient counts in the energy range from ~7 to ~17 eV, then the high-energy-electron moments calculations exclude all the channels below that minimum. If a large energy is found for this minimum (100 eV or above), we

further require that there be appreciable counts at high electron energies as well (>100 counts averaged over upper 10 energy channels); i.e., we require evidence of a strong surface-charging environment, which is necessary to produce a large barrier potential.

2k. Computation of flux and phase space density matrices

From the background-corrected count rates, C_{ijk}, the differential flux F is computed within the warm plasma approximation (i.e., that the distribution is uniform over the energy/angle response of the instrument):

$$F_{ijk}\ (cm^{-2}\ s^{-1}\ sr^{-1}\ eV^{-1}) = C_{ijk} / (\tau\ \varepsilon_{ij}\ G_j\ E_i) \quad ,$$

where C_{ijk} is the count rate measured by the jth detector at particle energy E_i and sweep number k, ε_{ij} is the efficiency of detector j at energy E_i, G_j is the geometric factor of detector j, and τ is the sample accumulation time (0.009 sec). The energy E_i is given in eV.

The phase space density is derived from the differential flux:

$$f = (m^2 / 2E)\ F \quad ,$$

which gives

$$f_{ijk}\ (cm^{-6}\ s^3) = K_s\ F_{ijk}\ (cm^{-2}\ s^{-1}\ sr^{-1}\ eV^{-1}) / E_i\ (eV) \quad ,$$

where for electrons the species-specific constant K_s ($=m^2/2$ in appropriate units) is

$$K_s = K_e = 1.616 \times 10^{-31}\ (eV^2\ cm^{-4}\ s^4) \quad ,$$

and for ions (assuming all ions are protons) it is

$$K_s = K_p = 5.449 \times 10^{-25}\ (eV^2\ cm^{-4}\ s^4) \quad .$$

2l. Correction of energies for the spacecraft potential

As discussed above, surface charging of the spacecraft causes incident particles to gain or lose energy as they pass through the potential sheath around the spacecraft. The measured energy of a given particle, E, is related to its energy at infinity (i.e., outside the spacecraft sheath), E', by

$$E = E' - q\Phi_{sc} \quad ,$$

where q is the particle charge, and Φ_{sc} is the spacecraft potential (see section 2i). Ions (q=+1) are accelerated (E > E') as they approach a negatively charged spacecraft ($\Phi_{sc} < 0$) and electrons (q=-1) are similarly decelerated. Neglecting sheath asymmetries and focusing (i.e., assuming that the instrument is a point at the center of a completely spherical potential well), a particle's velocity-space coordinates in the ambient medium are related to its measured velocity by

$$v' = (2E' / m)^{1/2} = [2(E + q\Phi_{sc}) / m]^{1/2} \quad , \qquad (4a)$$

$$\theta' = \theta \quad , \tag{4b}$$

$$\phi' = \phi \quad , \tag{4c}$$

where θ and ϕ are, respectively, the polar angle and azimuth of the particle velocity vector. These angles are related to θ and ϕ, the polar angle and azimuth of incidence measured at the instrument, by

$$\theta = 180^\circ - \theta$$

and $$\phi = \phi + 180^\circ \quad .$$

2m. Computation of sums

Calculation of the moments (Equations 1) involves integrating the phase space density, weighted by various functions of the particle velocity, over velocity space:

$$M_n = \int f(\mathbf{v}')\, g_n(\mathbf{v}')\, d^3\mathbf{v}'$$

$$= \int dv' \int d\phi' \int d\theta'\, v'^2 \sin\theta'\, f(\mathbf{v}')\, g_n(\mathbf{v}') \quad .$$

This integration refers to the velocity-space properties in the ambient medium, which are related to those measured at the satellite by Equations 4.

The weighting functions g_n needed for the moments in Equations 1 are separable functions of the three velocity-space coordinates:

$$g_n(\mathbf{v}') = V_n(v')\, \Theta_n(\theta')\, \Phi_n(\phi') \quad .$$

The functions V_n, Θ_n, and Φ_n are listed in Table 7.

Under the assumption that the distribution function is uniform over a particular velocity-space element ($\Delta\theta'$, $\Delta\phi'$, $\Delta v'$), the integral moments M_n can be approximated as weighted sums of the phase space density over finite velocity-space elements:

$$M_n \approx M_n = \Sigma_i \Sigma_j \Sigma_k\, (f'_{ijk}) \left[\int_i dv'\, v'^2\, V_n(v') \right]$$

$$\times \left[\int_j d\theta'\, \sin\theta'\, \Theta_n(\theta') \right] \left[\int_k d\phi'\, \Phi_n(\phi') \right]$$

$$= \Sigma_i \Sigma_j \Sigma_k\, (f'_{ijk})\, V_{ni}\, Q_{nj}\, F_{nk} \quad . \tag{5}$$

In this equation $\int_i$ represents the integration over the ith v'-cell, with limits v'_{i1} to v'_{i2}, and similarly for $\int_j$ and $\int_k$. By Equations 4b and 4c, $\theta'_{j1} = \theta_{j1}$, $\theta'_{j2} = \theta_{j2}$, $\phi'_{k1} = \phi_{k1}$, and

Table 7. Moment Functions

n	M_n	$V_n(v')$	$\Theta_n(\theta)$	$\Phi_n(\phi)$
1	n	1	1	1
2	nv_x	v	$\sin\theta$	$\cos\phi$
3	nv_y	v	$\sin\theta$	$\sin\phi$
4	nv_z	v	$\cos\theta$	1
5	nv_xv_x	v^2	$\sin^2\theta$	$\cos^2\phi$
6	nv_xv_y	v^2	$\sin^2\theta$	$\cos\phi \sin\phi$
7	nv_xv_z	v^2	$\sin\theta \cos\theta$	$\cos\phi$
8	nv_yv_y	v^2	$\sin^2\theta$	$\sin^2\phi$
9	nv_yv_z	v^2	$\sin\theta \cos\theta$	$\sin\phi$
10	nv_zv_z	v^2	$\cos^2\theta$	1

$\phi'_{k2} = \phi_{k2}$. Moreover, by Liouville's theorem, the phase space density is conserved along dynamical trajectories, so

$$f'_{ijk} = f(\mathbf{v}') = f(\mathbf{v}) = f_{ijk} \quad ,$$

where $\mathbf{v}$ and $\mathbf{v}'$ are related by Equations 4. Thus, the moment sums of Equation 5 may be written as

$$M_n = \Sigma_i \Sigma_j \Sigma_k f_{ijk}(v_i,\theta_j,\phi_{ik})\, V_{ni}\, Q_{nj}\, F_{nik} \quad , \qquad (6)$$

where f_{ijk} is the phase space density derived as described above (section 2k) from the count rate C_{ijk} measured by the jth detector (viewing particles with polar angle θ_j at a look direction of θ_j=180°-θ_j) at particle speed v_i, and azimuth ϕ_{ik} (corresponding to look azimuth ϕ_{ik}=ϕ_{ik}-180°, defined above in Equation 2). The integrated elements V_{ni}, Q_{nj}, and F_{nik} are listed in Table 8. Note that V_{ni} must still be evaluated at the free-space limits v'_{i1} and v'_{i2}, which are related to the energy channel edges according to Equation 4a.

The expressions for F_{nik} in Table 8 take advantage of the fact that the range of azimuth ϕ_{ik1} to ϕ_{ik2} is centered on ϕ_{ik}; i.e.,

$$\phi_{ik1} = \phi_{ik} - \Delta\phi / 2$$

and

$$\phi_{ik2} = \phi_{ik} + \Delta\phi / 2 \quad .$$

The quantities $\Delta\theta$ and $\Delta\phi$ in Table 8 are

$$\Delta\phi = 0.2618 \text{ rad}$$

and $$\Delta\theta = 0.4014 \text{ rad} \quad ,$$

corresponding to 15° and 23°, respectively.

Note that the approximation of the integral moments M_n as weighted sums over finite velocity-space elements centered on the actual measurement points requires that the measurements occur on a regular grid in velocity space. For MPA the cadence of the energy sweeps (one every 423 msec) gives fairly even azimuth coverage at a spin period of 10.15 ± 0.10 sec (actual spin periods so far have been in the range 9.95-10.15 sec). At spin periods much different from this, the measurements would probably need to be interpolated to a more regular azimuth grid.

The sums in Equation 6 extend over all 6 detectors (j) and all 24 azimuthal sectors (each corresponding to a single energy sweep, k). The sum over the energy channels, i, is restricted to certain ranges, depending on the target population. For low-energy ions, the sum ranges from i=23 to 40 (corresponding to the approximate energy range of 1-100 eV). For high-energy ions the range is i=1,22 (~100 eV - ~45 keV), and for the high-energy electrons it is i=1,27 (~30 eV - ~45 keV).

Table 8. Integrated Moment Elements

n	M_n	V_{ni}	Q_{nj}	F_{nik}
1	n	$(v'_{i2}{}^3 - v'_{i1}{}^3)/3$	$\cos\theta_{j1} - \cos\theta_{j2}$	$\Delta\phi$
2	nv_X	$(v'_{i2}{}^4 - v'_{i1}{}^4)/4$	$\Delta\theta/2 - (\sin2\theta_{j2} - \sin2\theta_{j1})/4$	$2\cos\phi_{ik} \sin(\Delta\phi/2)$
3	nv_Y	V_{2i}	Q_{2j}	$2\sin\phi_{ik} \sin(\Delta\phi/2)$
4	nv_Z	V_{2i}	$(\sin^2\theta_{j2} - \sin^2\theta_{j1}) / 2$	F_{1ik}
5	nv_Xv_X	$(v'_{i2}{}^5 - v'_{i1}{}^5)/5$	$[\cos\theta_{j1} (\sin^2\theta_{j1} + 2)$ $- \cos\theta_{j2} (\sin^2\theta_{j2} + 2)] / 3$	$\Delta\phi/2 + (1 - 2\sin^2\phi_{ik})$ $\cdot \sin(\Delta\phi/2) \cos(\Delta\phi/2)$
6	nv_Xv_Y	V_{5i}	Q_{5j}	$2 \sin\phi_{ik} \cos\phi_{ik}$ $\cdot \sin(\Delta\phi/2) \cos(\Delta\phi/2)$
7	nv_Xv_Z	V_{5i}	$(\sin^3\theta_{j2} - \sin^3\theta_{j1}) / 3$	F_{2ik}
8	nv_Yv_Y	V_{5i}	Q_{5j}	$\Delta\phi/2 - (1 - 2\sin^2\phi_{ik})$ $\cdot \sin(\Delta\phi/2) \cos(\Delta\phi/2)$
9	nv_Yv_Z	V_{5i}	Q_{7j}	F_{3ik}
10	nv_Zv_Z	V_{5i}	$(\cos^3\theta_{j1} - \cos^3\theta_{j2}) / 3$	F_{1ik}

2n. Interpolation across polar gaps

As mentioned above, MPA measures the full distribution to within 21° of the spin axis, thus leaving holes along the spin axis that total 6.6% of the unit sphere. To estimate the contribution of these unmeasured "polar gaps" to the various moment sums, we approximate the distribution at polar angles of 0° and 180° by the spin-averaged values obtained from detectors 6 and 1, respectively:

$$M_n^{\text{polar gap}} = \Sigma_i \left[f_{i0}\, V_{ni}\, A_{n0} + f_{i180}\, V_{ni}\, A_{n180} \right] \quad , \qquad (7)$$

where

$$f_{i0} = \left[\Sigma_k f_{i,j=6,k} \right] / 24 \quad ,$$

$$f_{i180} = \left[\Sigma_k f_{i,j=1,k} \right] / 24 \quad ,$$

$$A_{n0} = \int d\phi \int d\theta \sin\theta\, \Theta_n(\theta)\, \Phi_n(\phi) \qquad \phi = 0,360^\circ;\ \theta = 0,21^\circ \quad ,$$

$$A_{n180} = \int d\phi \int d\theta \sin\theta\, \Theta_n(\theta)\, \Phi_n(\phi) \qquad \phi = 0,360^\circ;\ \theta = 159,180^\circ \quad .$$

The functions $\Theta_n(\theta)$ and $\Phi_n(\phi)$ are defined in Table 7, and V_{ni} is defined in Table 8. The full estimated moments are then the sum of the piece estimated from the observations directly (Equation 6) and the estimated polar-gap piece (Equation 7):

$$M_n = M_n + M_n^{\text{polar gap}} \quad .$$

2o. Combination of sums to yield moments

The desired moments (Equations 1) are derived by combining the various sums M_n described above. The density and velocity of each population are determined in a straightforward manner. With the speeds v'_{i1} and v'_{i2} given in units of cm/s, we have

$$n\ (\text{cm}^{-3}) \approx M_1$$

$$\mathbf{V}\ (\text{km/s}) \approx 10^{-5}\, (M_2, M_3, M_4) / M_1 .$$

The calculation of the temperature involves a bit more work. First, noting that

$$\mathbf{T} = (1 / n) \int m\, (\mathbf{v}-\mathbf{V})\, (\mathbf{v}-\mathbf{V})\, f(\mathbf{v})\, d^3\mathbf{v}$$

$$= \left[(1 / n) \int m\, \mathbf{vv}\, f(\mathbf{v})\, d^3\mathbf{v} \right] - \mathbf{VV} \quad ,$$

we form the symmetric matrix **UU**, where

$$UU_{11} = (M_5 / M_1) - (M_2 / M_1)^2 \quad ,$$

$$UU_{12} = UU_{21} = (M_6 / M_1) - (M_2\, M_3) / M_1^2 \quad ,$$

$$UU_{13} = UU_{31} = (M_7 / M_1) - (M_2\, M_4) / M_1^2 \quad ,$$

$$UU_{22} = (M_8 / M_1) - (M_3 / M_1)^2 \ ,$$

$$UU_{23} = UU_{32} = (M_9 / M_1) - (M_3\, M_4) / M_1^2 \ ,$$

$$UU_{33} = (M_{10} / M_1) - (M_4 / M_1)^2 \ .$$

This symmetric matrix is diagonalized, yielding the three eigenvalues (u_1, u_2, u_3), ordered in ascending value, and their corresponding eigenvectors $\mathbf{U}_1$, $\mathbf{U}_2$, $\mathbf{U}_3$. The eigenvalues are converted to temperature units according to

$$T_n\ (eV) = c_s\, u_n \ ,$$

where $c_s = c_p = (1.042 \times 10^{-12}$ g eV/erg)

and $c_s = c_e = (5.686 \times 10^{-16}$ g eV/erg)

are used for the ions and electrons, respectively. Then the direction angles θ_n and ϕ_n corresponding to each eigenvector are determined.

Finally, ratios of the three temperature eigenvalues are computed and compared to see which two eigenvalues are the most similar and therefore correspond to $T_\perp$ under the assumption of gyrotropy; $T_\perp$ is defined as the average of these two eigenvalues. The remaining eigenvalue is identified as $T_\parallel$, and its associated eigenvector is identified as the magnetic field direction. From this eigenvector, we determine the polar angle θ_B from the spin axis of the satellite and the azimuth angle ϕ_B, which is referenced to the plane containing the spin axis and geographic north. Because there is an intrinsic 180° ambiguity in the direction of the magnetic field (since we find only the symmetry axis of the distribution), we assume that the field is basically northward and choose the appropriate value of θ_B based on whether ϕ_B is found in the southern or northern hemisphere. The quality of this determination can be checked by examining the value of the ratio of $T_\perp$ to the middle eigenvalue (T_2) of the temperature matrix. This ratio will be very close to 1 for a good determination.

3. Reported Products

The coordinate system for the reported products is spacecraft-centered: the z-axis points along the spin axis toward Earth's center; the x-axis lies in the plane containing the spin axis and geographic north; and the y-axis completes the set, pointing basically in the eastward direction. The units for the densities, velocities, temperatures, and fluxes are [cm^{-3}], [km s^{-1}], [eV], and [cm^{-2} s^{-1} sr^{-1} eV^{-1}], respectively. Angles are given in degrees.

From the production run of the moments code, there are five different output data files: one VAX binary file, two ASCII files, and two cdf files. Except for the cdf files, the

file names all follow the convention satellite-name_date.type (for example, 1991-080_23-JUN-1992.moments). The cdf files use the naming convention required by the NASA International Solar-Terrestrial Physics (ISTP) project; for example, L7_k0_mpa_19981211_v02.cdf is the key parameter file submitted to ISTP containing data from satellite LANL-97A from December 11, 1998, with moments computed using the new version (v02) of the moments code (as described in this document).

The final data products contained in these various files are the following:

3.1 Archival VAX binary files (sat-name_date.moments)

Low-Energy Ions (~1-100 eV):

n, V_x, V_y, V_z, T_1, T_2, T_3, θ_1, θ_2, θ_3, ϕ_1, ϕ_2, ϕ_3

High-Energy Ions (~100 eV - 45 keV):

n, V_x, V_y, V_z, T_1, T_2, T_3, θ_1, θ_2, θ_3, ϕ_1, ϕ_2, ϕ_3, $T_{\|}$, $T_{\perp}$, θ_B, ϕ_B

High-Energy Electrons (~30 eV - 45 keV):

n, V_x, V_y, V_z, T_1, T_2, T_3, θ_1, θ_2, θ_3, ϕ_1, ϕ_2, ϕ_3, $T_{\|}$, $T_{\perp}$, θ_B, ϕ_B

Ephemeris and Ancillary Data:

UT [hours]

Geographic Local Time [hours] (defined as UT + geographic longitude)

Satellite name

Date

Geographic x,y,z location of satellite [km]

Dipole magnetic latitude

Spacecraft magnetic latitude and magnetic local time (calculated from the Geopack software package from Goddard Space Flight Center)

Quality Flags

inv_mf_mpa = no. of invalid main frames in the current record

pack_flags = 4-byte integer, where each byte is a flag, with values as follows:

IPFLAG

0 spacecraft potential from iteration

1 spacecraft potential from ion line

2 real zero for spacecraft potential

3 real zero and ion line found; potential from ion line

IBFLAG

1 barrier at or below 30 eV; set to 30 eV

2 barrier between 30 and 400 eV with low confidence

3 barrier between 30 and 400 eV with good confidence

4 barrier may be above 400 eV; set to 400 eV

IQUAL1

9 good ephemeris, good zero yaw

10 calculated ephemeris, good zero yaw

12 bad ephemeris, good zero yaw

17 good ephemeris, calculated zero yaw

18 calculated ephemeris, calculated zero yaw

20 bad ephemeris, calculated zero yaw

33 good ephemeris, bad zero yaw

34 calculated ephemeris, bad zero yaw

36 bad ephemeris, bad zero yaw

IQUAL2=Version Number (=2)

Spacecraft spin period [sec]

Spacecraft potential [volts]

Barrier energy [eV] (energy of lowest channel included in electron moment sums)

Penetrating background, b_{ave}, [counts / 9-ms]

Logarithmic center energies of electron and ion channels (-1.0 for channels above maximum HVPS level)

Geometric factors [cm^2 sr] and relative efficiencies for the 6 detectors

Spin-averaged fluxes from detectors 3 and 4 at each ion and electron energy level

3.2 ASCII files for Unix workstation access and storage (sat-name_date.ascii_moments)

Low-Energy Ions (~1-100 eV):

$n, V_x, V_y, V_z, T_1, T_2, T_3, \theta_1, \theta_2, \theta_3, \phi_1, \phi_2, \phi_3$

High-Energy Ions (~100 eV - 45 keV):

$n, V_x, V_y, V_z, T_1, T_2, T_3, \theta_1, \theta_2, \theta_3, \phi_1, \phi_2, \phi_3, T_{\|}, T_{\perp}, \theta_B, \phi_B$

High-Energy Electrons (~30 eV - 45 keV):

$n, V_x, V_y, V_z, T_1, T_2, T_3, \theta_1, \theta_2, \theta_3, \phi_1, \phi_2, \phi_3, T_{\|}, T_{\perp}, \theta_B, \phi_B$

Ephemeris and Ancillary Data:

UT [hours]

Geographic Local Time [hours] (defined as UT + geographic longitude)

Satellite name

Date

Geographic x,y,z location of satellite [km]

Dipole magnetic latitude

Spacecraft magnetic latitude and magnetic local time (calculated from the Geopack software package from Goddard Space Flight Center)

Quality Flags

inv_mf_mpa = number of invalid main frames in the current record

flag_arr = flag array, defined as follows

flag_arr(1) = IPFLAG (see 3.1 above)

flag_arr(2) = IBFLAG (see 3.1 above)

flag_arr(3) = IQUAL1 (see 3.1 above)

flag_arr(4) = IQUAL2 (see 3.1 above)

Spacecraft spin period [sec]

Spacecraft potential [volts]

Barrier energy [eV] (energy of lowest channel included in electron moment sums)

Penetrating background, b_{ave}, [counts / 9-ms]

Logarithmic center energies of electron and ion channels (-1.0 for channels above maximum HVPS level)

Geometric factors [cm^2 sr] and relative efficiencies for the 6 detectors

Spin-averaged fluxes from detectors 3 and 4 at each ion and electron energy level

3.3 ASCII files for VAX access (sat-name_date.macmom)

Low-Energy Ions (~1-100 eV):

n, V_x, V_y, V_z, T_1, T_2, T_3, θ_1, θ_2, θ_3, ϕ_1, ϕ_2, ϕ_3

High-Energy Ions (~100 eV - 45 keV):

n, V_x, V_y, V_z, T_1, T_2, T_3, θ_1, θ_2, θ_3, ϕ_1, ϕ_2, ϕ_3, $T_{\|}$, $T_{\perp}$, θ_B, ϕ_B

High-Energy Electrons (~30 eV - 45 keV):

n, V_x, V_y, V_z, T_1, T_2, T_3, θ_1, θ_2, θ_3, ϕ_1, ϕ_2, ϕ_3, $T_{\|}$, $T_{\perp}$, θ_B, ϕ_B

Ephemeris and Ancillary Data:

UT [hours]

Geographic Local Time [hours] (defined as UT + geographic longitude)

Satellite name

Year, Day of Year

Geographic x,y,z location of satellite [km]

Spacecraft magnetic latitude and magnetic local time (calculated from the Geopack software package from Goddard Space Flight Center)

Quality Flags

flag_arr = flag array

flag_arr(1) = IPFLAG (see 3.1 above)

flag_arr(2) = IBFLAG (see 3.1 above)

flag_arr(3) = IQUAL1 (see 3.1 above)

mac_temp = quality flag

0 nominal

1 nonzero invalid main frame counter and/or >10 bcbc replacements

Spacecraft potential [volts]

Barrier energy [eV] (energy of lowest channel included in electron moment sums)

Penetrating background, b_{ave}, [counts / 9-ms]

Penetrating background for ions (same as b_{ave}), electrons

Highest valid ion, electron energy

Spin-averaged fluxes from detectors 3 and 4 at top 10 ion and electron energy levels

3.4 Key Parameter CDF files for transmission to the ISTP CDHF
(e.g., L7_k0_mpa_19981211_v02.cdf)

Low-Energy Ions (~1-100 eV):

n, V_x, V_y, V_z, $T_{||}$, $T_{\perp}$, $T_{\perp}/T_2$

High-Energy Ions (~100 eV - 45 keV):

n, V_x, V_y, V_z, $T_{||}$, $T_{\perp}$, $T_{\perp}/T_2$, θ_B, ϕ_B

High-Energy Electrons (~30 eV - 45 keV):

n, $T_{||}$, $T_{\perp}$, $T_{\perp}/T_2$, θ_B, ϕ_B

Ephemeris and Ancillary Data:

Date, time

Spacecraft position (altitude, geographic latitude, geographic longitude)

Magnetic latitude and magnetic local time

Spacecraft potential [volts]

Penetrating background, b_{ave}, [counts / 9-ms]

Qual_flag

0 Good or good calculated zero yaw

1 Bad zero yaw

Gap_flag

0 No data gap greater than 5 minutes

1 Data gap greater than 5 minutes

3.5 High-resolution CDF files for storage on CD-ROM
(e.g., L7_h0_mpa_19981211_v02.cdf)

Low-Energy Ions (~1-100 eV):

n, V_x, V_y, V_z

High-Energy Ions (~100 eV - 45 keV):

n, $T_\perp$, $T_\parallel$, θ_B, ϕ_B

High-Energy Electrons (~30 eV - 45 keV):

n, $T_\perp$, $T_\parallel$, θ_B, ϕ_B

Full Distribution

Azimuthal angles of direction of motion for ions and electrons at each energy level and azimuthal bin, ϕ_{ik}

Background-corrected counts for ions and electrons, $(C_{ijk}-b_j)$ (cts / 9-ms)

Ephemeris and Ancillary Data:

Energy-dependent efficiency at each ion and electron energy level

Geometric factors for each detector

Channel center energies

Polar angle ranges covered

Date, time

Spacecraft position (geographic x,y,z [km])

Magnetic latitude and magnetic local time

Penetrating background for each detector (from ions) [counts / 9-ms]

Penetrating background for each detector (from electrons) [counts / 9-ms] (used for background correction only if it is less than twice the ion background)

Spacecraft potential [volts]

Flags

Invalid main frame count

pack_flags (see 3.1 above)

Acknowledgments: We would like to thank our colleagues on the MPA team for their interest, help, and encouragement in this task. Special thanks to Rod Christensen for the calculation of missing satellite ephemeris data and to Sylvestre Maurice for writing the algorithm to reconstruct the zero-yaw time. This work was carried out under the auspices of the U. S. Department of Energy.

References

Bame, S. J., et al., Magnetospheric plasma analyzer for spacecraft with constrained resources, *Rev. Sci. Instrum.*, *64*, 1026, 1993.

Gosling, J. T., M. F. Thomsen, and R. C. Anderson, A Cookbook for Determining Essential Transmission Characteristics of Spherical Section Electrostatic Analyzers, *LA-10147-M*, Los Alamos National Laboratory, 1984.

Lawrence, D. J., M. F. Thomsen, J. E. Borovsky, and D. J. McComas, Measurements of early and late-time plasmasphere refilling, *J. Geophys. Res.*, in press, 1999.

McComas, D. J., et al., Magnetospheric plasma analyzer: Initial three-spacecraft observations from geosynchronous orbit, *J. Geophys. Res.*, *98*, 13453, 1993.

Thomsen, M. F., D. J. McComas, G. D. Reeves, and L. A. Weiss, An observational test of the Tsyganenko (T89a) model of the magnetospheric field, *J. Geophys. Res.*, *101*, 24, 1996.